Supporting information for

Revisit ion transport through micropores: significant and non-negligible surface transport

Wenchang Zhang[1#], Ao Zhang[2#], Wenzhe Zhou[1], Yu Ji[1], Zhiping Xu[2], Pengzhan Sun[1*]

[1]Institute of Applied Physics and Materials Engineering, University of Macau, Macau SAR 999078, P. R. China

[2]Applied Mechanics Laboratory, Department of Engineering Mechanics and Center for Nano and Micro Mechanics, Tsinghua University, Beijing 100084, P. R. China

Device fabrication

Commercially supplied Si wafers (~ 500 μm thick) coated with either 500 nm- or 300 nm-thick SiN_x layers on both sides (from *SIEGERT WAFER GmbH*) were used for fabricating freestanding SiN_x membranes. Specifically, an array of squares of 800 μm in size were defined by photolithography on one side of the SiN_x wafer, followed by completely removing the exposed SiN_x by reactive ion etching (RIE). After dissolving the polymer mask, the processed wafer was immersed in a concentrated KOH solution (30 wt% in water) to etch away the exposed Si in the squares. The etching procedure lasted for 8 h at 80 °C, which produced an array of freestanding SiN_x membranes on the other side of the wafer, each about 100 μm in size. After thoroughly washing the wafer with acetic acid and deionized water, pores having diameters D of 0.2 ~ 5 μm were perforated on the freestanding SiN_x membranes using focused ion beam (FIB, from *ZEISS*), as exemplified in Fig. 1d.

To fabricate control pore devices with their outer SiN_x surfaces covered by monolayers of graphene, graphene oxide (GO) and titania nanosheets, respectively, we employed SiN_x pores of ~2 μm in diameter. Large-area and continuous monolayer graphene films were prepared by the well-established chemical vapour deposition (CVD)[1,2]. Monolayers of GO and titania were prepared by the modified Hummer's method[3,4] and chemical exfoliation method[5-7], respectively. The latter two samples had lateral dimensions of a few to a few tens of μm and thicknesses of about 1 nm, in consistent with most previous studies reported before. They were transferred on top of the SiN_x pores using methods standard for van der Waals assembly[8,9] and thin layers of spin-coated poly(methyl methacrylate) (PMMA, 4 wt% in anisole, from *Microchem*) as mechanical supports. Most of the resulting freestanding 2D membranes spanning over the pores' top were broken after dissolving the polymer with acetone, thoroughly rinsing with isopropanol and blow-drying using nitrogen gun, leaving only the pores' outer surfaces covered by the selected 2D crystals. Characterizations for the final devices are shown in Fig. S1.

For contact angle measurements, SiN_x surfaces covered by sufficiently large-area and dense 2D films are required. To this end and in addition to bare SiN_x substrate and that covered by CVD-graphene, monolayers of GO and titania nanosheets were deposited onto SiN_x wafers by the well-established Langmuir–Blodgett assembly technique[10,11], thanks to the rich negative surface charges on the basal planes[11-13]. Fig. S2a shows the transferred CVD-graphene film. Occasionally, cracks and wrinkles were present on the resulting samples. Fig. S2b shows one of our deposited GO films. Because of similar morphologies of individual GO and titania sheets (Figs. S2b and c), surfaces with deposited titania sheets were quite similar to those deposited

with GO sheets.

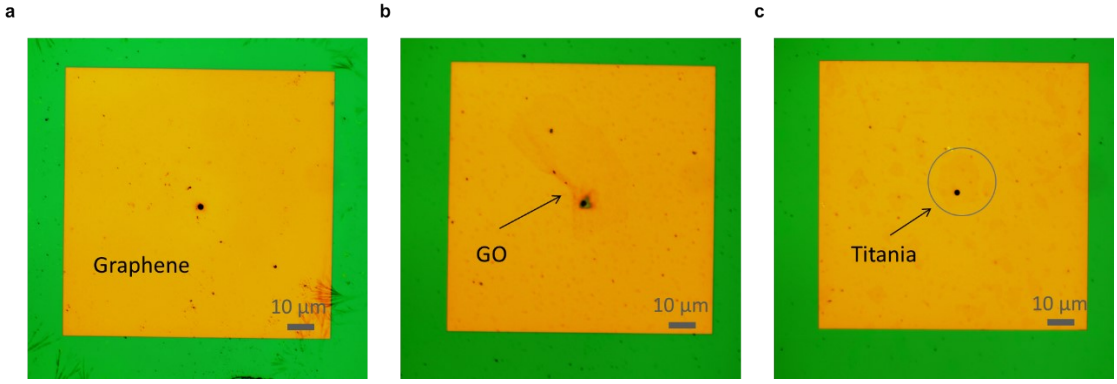

Fig. S1 Optical images for 2D crystals placed on the surface of SiN_x pore. a, CVD-graphene film **b,** GO sheet **c,** titania sheet on the surface of SiN_x pore. The grey circle in the image c indicates the location of the titania sheet.

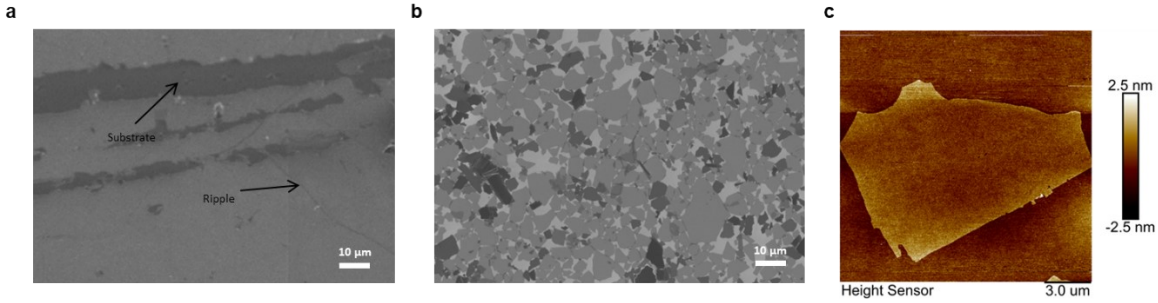

Fig. S2 The characterization of nanomaterials. FE-SEM image of **a,** single-layer graphene **b,** graphene oxide coated on the bare SiN_x substrate. **c,** AFM images of titanium dioxide nanosheets.

Finite element analysis

Trying to understand the spatial distribution of ion current under an applied electric field in our experimental setup (Fig. 1), we performed finite element analysis using the FEniCS software.[14] The simulations solved the Poisson–Nernst–Planck (PNP) equations for KCl solutions with concentrations of K^+ and Cl^- being c^+ and c^-, respectively, and under an applied voltage V:

$$\nabla \cdot (-\epsilon \nabla V) = F(c^+ - c^-) \quad \text{S1}$$

$$\nabla \cdot \left(-\nabla c^{\pm} \mp \frac{e}{k_B T} c^{\pm} \nabla V\right) = 0 \quad \text{S2}$$

where ϵ, F, e, k_B and T are the dielectric constant of water, Faraday constant, elementary charge, Boltzmann constant, and temperature, respectively. The simulation domain is schematically shown in the inset of Fig. S5a, which is cylindrical with y-axis the axis of symmetry. The domain has a radius of AB = 5 µm and consists of two reservoirs separated by a solid-state wall (the model device). Each reservoir has a height of BC = FG = 5 µm, and the device has a thickness of DE = 0.5 µm. A pore is located at the center of the device. Its radius r (MD) ranges from 0.2 to 2 µm. Dirichlet boundary conditions for voltage and concentration were applied at the boundaries AB and GH, with $V_{AB} - V_{GH} = 0.1$ V and $c_{AB} = c_{GH} = c_{bulk}$ (C in the

main text). Three bulk concentrations were considered, c_{bulk} (C) = 0.01 mM, 0.01 M or 0.1 M. A boundary condition of surface charge density $\sigma = \epsilon \partial V/\partial n$ was applied to the device's surfaces CD, DE, and EF, where n is the outer normal and the surface charge density σ = 0.01 or 0.02 C/m² (typical for a SiN_x surface). The side boundaries BC and GF were treated with natural boundary conditions.

First-order Lagrange elements and a non-uniform mesh were adopted for solving equations S1 and S2 based on finite element analysis. The mesh near the device was refined to ensure the local size was smaller than 0.3 nm, which is the typical Debye length for a 1-M KCl solution. We calculated the ion current from the computed ion concentration distribution using

$$\vec{j} = F\left(D^- \nabla c^- - D^+ \nabla c^+\right) - \frac{e}{k_B T} F \nabla V \left(c^+ D^+ + c^- D^-\right) \quad \text{S3}$$

The total current I_{total} was defined as the current through the pore's entire cross-section (with radius r = DM), whereas the edge current I_{edge} was defined as the current crossing through DN. The spatial distribution of simulated current streamlines under different conditions of r, C and σ are shown in Figs. S3 and S4. The evolutions of I_{total} and I_{edge} as a function of r under different C and σ are shown in Fig. S5.

Usually, in simulations of micro or nanopores the reservoirs are much larger than the pore diameter and the reservoir is hemi-spherical (to better accommodate the $1/r^2$ decay of the electric field).[15,16] Then we have performed additional finite element simulations to show that the size of the reservoir did not have a noticeable impact on the current distribution in the pore. In those simulations, the pore had a radius of 0.1 μm and a height of 10 nm, and the reservoir sizes were set as 0.25 μm, 0.5 μm, 1 μm, and 2 μm respectively. Other conditions remained the same as Fig. S4. The results have been summarized as a Fig. S6. It is seen that varying the reservoir size resulted in negligible differences in the current distribution. Accordingly, the conditions used in Fig. S4, that is, the reservoir size of 5 μm and no smaller than 2.5 times the pore radius, should be large enough. Studies using cylindrical reservoirs have also been frequently reported.[17,18] The effect of reservoir shape in our simulations was negligible because the resistance of the bulk solution was small compared to that of the pore and the voltages near the surfaces of either cylindrical or spherical reservoirs were approximately the same. The results are shown in Fig. S6.

Another important aspect is the use of simulations to explain why electroosmosis does not contribute to surface current. Herein, we have performed a finite element simulation with Stokes equation coupled with Poisson-Nernst-Planck equations and compared with that without considering the Stokes equation. To this end, the Stokes equation writes

$$\mu \nabla^2 \vec{u} - \nabla p - F\left(c^+ - c^-\right) \nabla V = 0 \quad \text{S4}$$

where the viscosity of water is μ=10^{-3} Pa·s. Also, we have the continuity equation $\nabla \cdot \vec{u} = 0$, and the Nernst-Planck equation becomes

$$\nabla \cdot \left(c^{\pm} \vec{u} - D \nabla c^{\pm} \mp \frac{De}{k_B T} c^{\pm} \nabla V \right) = 0. \quad \text{S5}$$

We have used the same conditions as in Fig. S6b, with free stress boundary conditions on boundaries AB and GH of Fig. S5a, and no-slip conditions on BC, CD, DE, EF and FG. The

streamlines and current density distributions for the pore size of 0.1 μm are summarized as Fig. S7. Without considering Stokes equation, the total current is 2.87 nA and the edge current is 2.73 nA. For comparison, by considering Stokes equation in our calculations, the total current is 2.81 nA and the edge current is 2.67 nA. Accordingly, we conclude that the effect of electroosmosis is insignificant. For the larger micropore with diameters notably larger than 0.1 μm, the ratio of Debye length to the pore radius becomes smaller and therefore, the effect of electroosmosis should be even smaller and can be safely neglected.

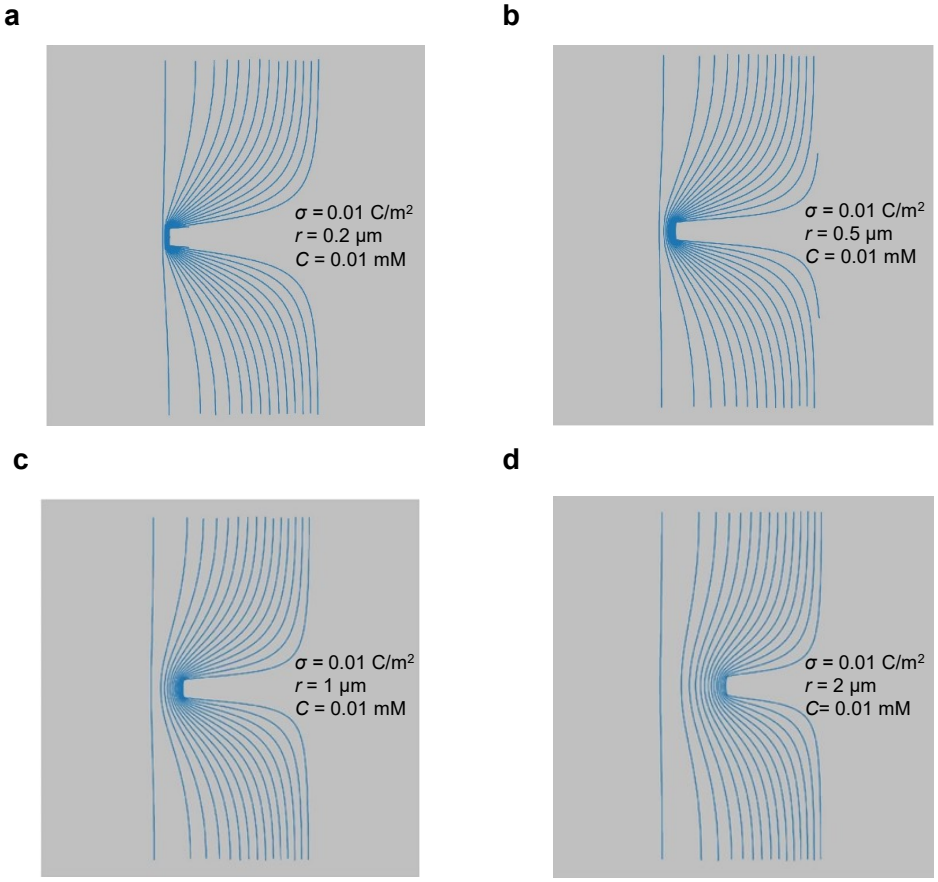

Fig. S3 The streamlines of ion current for solution concentration of 0.01 mM. Parameters for *r* and *σ* are specified in **a**-**d**. The current flow is equal between two adjacent streamlines.

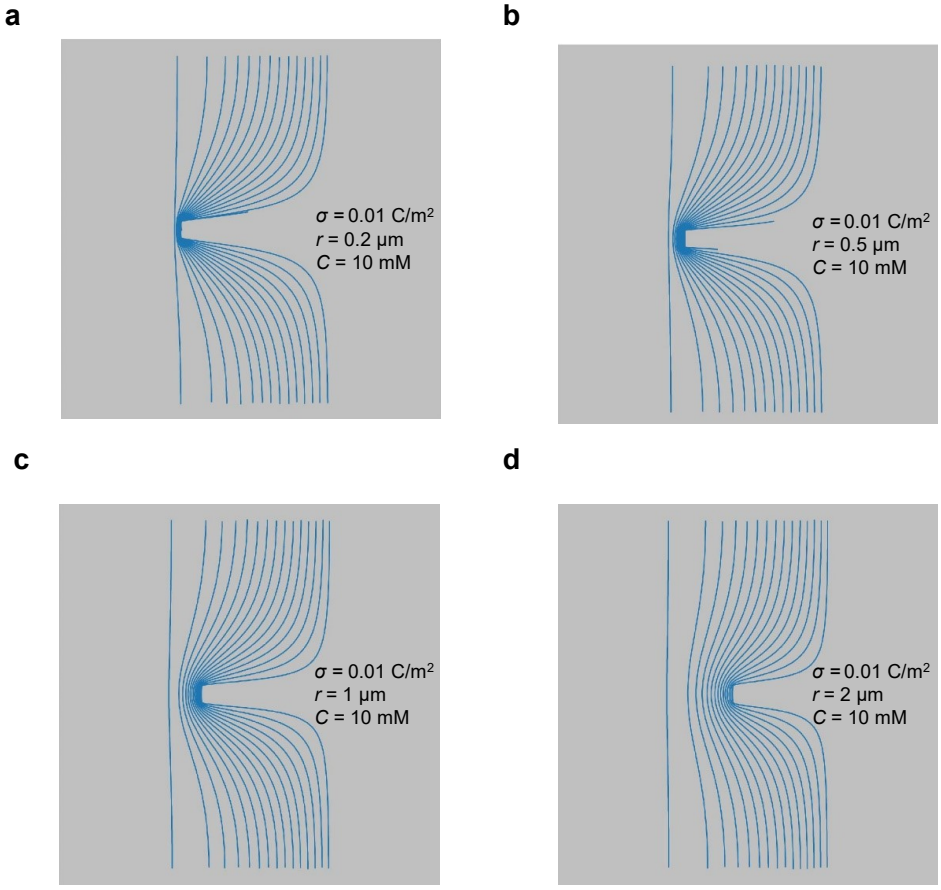

Fig. S4 The streamlines of ion current for solution concentration of 10 mM. Parameters for r and σ are specified in **a**-**d**. The current flow is equal between two adjacent streamlines.

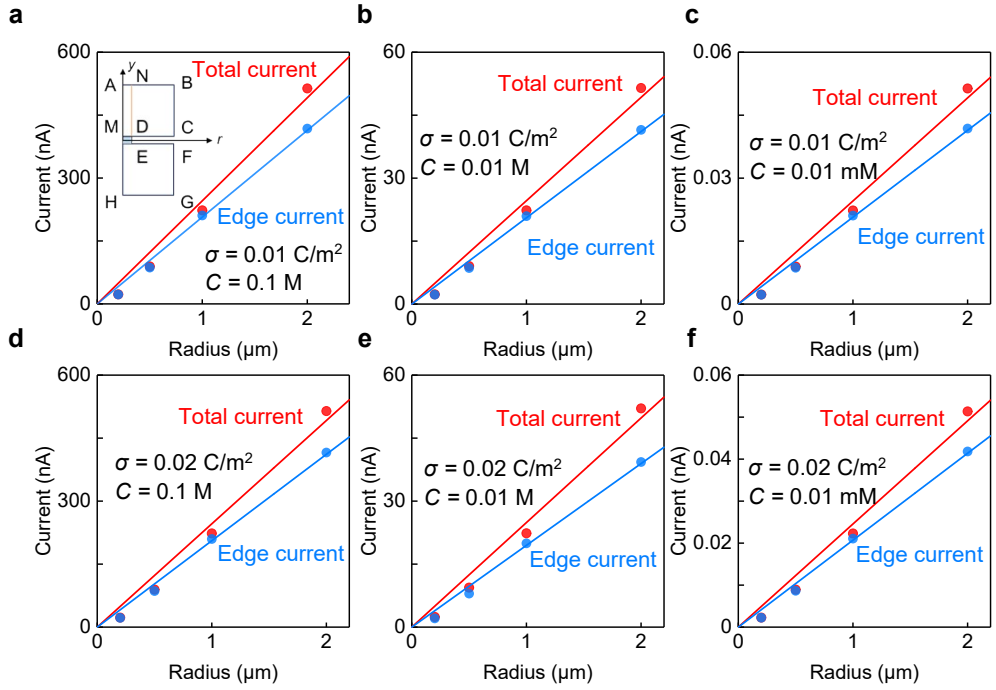

Fig. S5 Comparisons for the total and edge currents at different radii. Parameters for σ and C are specified in **a**-**f**. Symbols, calculations for I_{total} and I_{edge} (color-coded) at different r. Solid lines (same color-coding), best linear fits. Inset in (a), schematic for the simulation domain

with the pore shaded in blue.

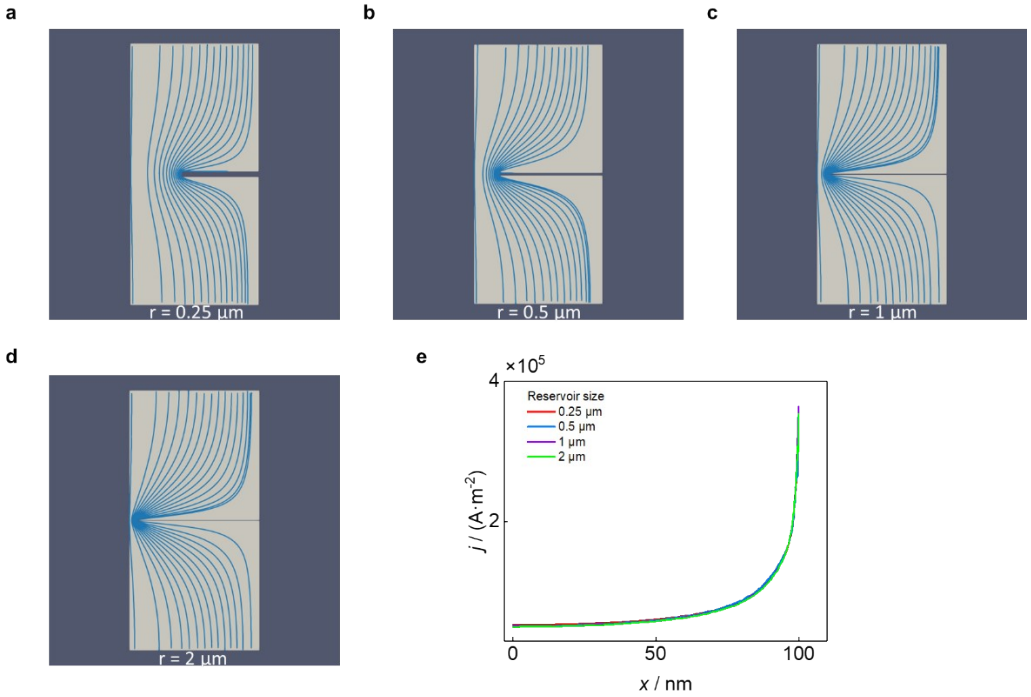

Fig. S6 a-d, The streamlines of ion current for solution concentration of 10 mM. The reservoir sizes are 0.25 μm, 0.5 μm, 1 μm, and 2 μm respectively. **e,** Current density distribution in the pore. *x* is the distance from the pore center.

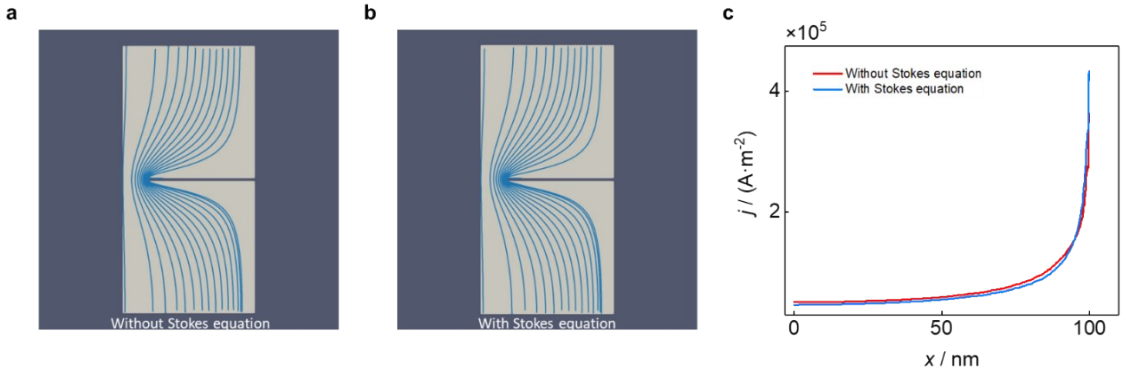

Fig. S7 a, b The streamlines of ion current, simulated without **a** and with **b** the Stokes equation. **c,** Current density in the pore, the red line represents finite element simulation without Stoke equation and the blue line represents finite element simulation with Stoke equation.

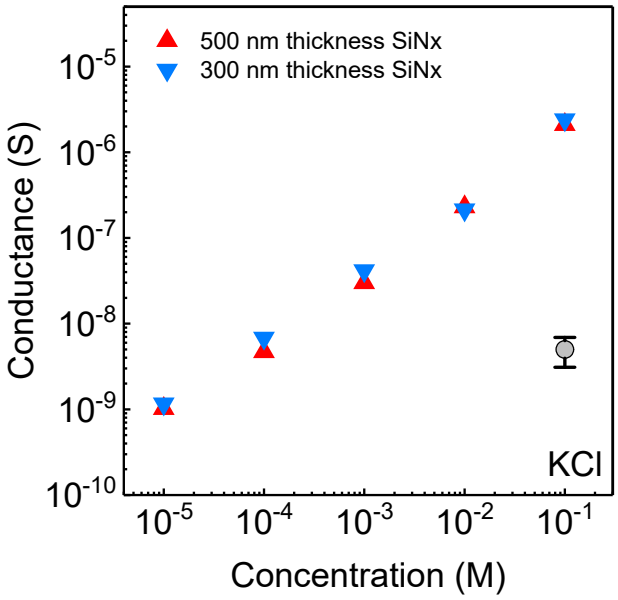

Fig. S8 Comparison of pore conductivity of SiN_x with two different aspect ratios. The red upper triangle represents a 500 nm thick SiN_x pore, and the blue lower triangle represents a 300 nm thick SiN_x pore. The pore diameter is 2 μm. The conductivity in KCl solution was tested.

References

1. A. Reina, X. Jia, J. Ho, D. Nezich, H. Son, V. Bulovic, M. S. Dresselhaus and J. Kong, *Nano Lett.*, 2009, **9**, 30–35.
2. A. Reina, S. Thiele, X. Jia, S. Bhaviripudi, M. S. Dresselhaus, J. A. Schaefer and J. Kong, *Nano Res.*, 2009, **2**, 509–516.
3. S. Stankovich, D. A. Dikin, R. D. Piner, K. A. Kohlhaas, A. Kleinhammes, Y. Jia, Y. Wu, S. T. Nguyen and R. S. Ruoff, *Carbon*, 2007, **45**, 1558–1565.
4. P. Sun, M. Zhu, K. Wang, M. Zhong, J. Wei, D. Wu, Z. Xu and H. Zhu, *ACS Nano*, 2013, **7**, 428–437.
5. T. Sasaki, M. Watanabe, H. Hashizume, H. Yamada and H. Nakazawa, *J. Am. Chem. Soc.*, 1996, **118**, 8329–8335.
6. T. Sasaki, Y. Ebina, Y. Kitami, M. Watanabe and T. Oikawa, *J. Phys. Chem. B*, 2001, **105**, 6116–6121.
7. T. Tanaka, Y. Ebina, K. Takada, K. Kurashima and T. Sasaki, *Chem. Mater.*, 2003, **15**, 3564–3568.
8. A. K. Geim and I. V. Grigorieva, *Nature*, 2013, **499**, 419–425.
9. L. Wang, I. Meric, P. Y. Huang, Q. Gao, Y. Gao, H. Tran, T. Taniguchi, K. Watanabe, L. M. Campos, D. A. Muller, J. Guo, P. Kim, J. Hone, K. L. Shepard and C. R. Dean, *Science*, 2013, **342**, 614–617.
10. A. Ulman, *An Introduction to Ultrathin Organic Films: From Langmuir–Blodgett to Self–Assembly*, Academic press, 2013.
11. K. Matsuba, C. Wang, K. Saruwatari, Y. Uesusuki, K. Akatsuka, M. Osada, Y. Ebina, R. Ma and T. Sasaki, *Sci. Adv.*, 2017, **3**, e1700414.
12. M. R. Karim, K. Hatakeyama, T. Matsui, H. Takehira, T. Taniguchi, M. Koinuma, Y.

Matsumoto, T. Akutagawa, T. Nakamura, S. Noro, T. Yamada, H. Kitagawa and S. Hayami, *J. Am. Chem. Soc.*, 2013, **135**, 8097–8100.
13. L. Wang and T. Sasaki, Chem. Rev., 2014, **114,** 9455–9486.
14. A. Logg, K.-A. Mardal and G. Wells, *Automated Solution of Differential Equations by the Finite Element Method: The FEniCS Book*, Springer Science & Business Media, 2012.
15. M. Baldelli, G. Di Muccio, A. Sauciuc, B. Morozzo della Rocca, F. Viola, S. Balme, A. Bonini, G. Maglia and M. Chinappi, *Adv. Mater.*, 2024, **36**, 2401761.
16. K. Willems, D. Ruić, F. L. R. Lucas, U. Barman, N. Verellen, J. Hofkens, G. Maglia and P. V. Dorpe, *Nanoscale*, 2020, **12**, 16775-16795.
17. J. H. Chaudhry, J. Comer, A. Aksimentiev and L. N. Olson, *Commun. Comput. Phys*., 2014, **15**, 93–125.
18. A. Kiy, S. Dutt, K. P. Gregory, C. Notthoff, M. E. Toimil-Molares and P. Kluth, Langmuir, 2024, **40**, 20888–20896.